Chemical Science

ROYAL SOCIETY OF CHEMISTRY

EDGE ARTICLE

View Article Online
View Journal

Cite this: DOI: 10.1039/d5sc09860b

All publication charges for this article have been paid for by the Royal Society of Chemistry

Unveiling structural forms of Ru in WO_x-template catalysts for efficient acidic PEM water electrolysis

Xiongfeng Zeng,†‡ Ao Cai,†‡ Junhui Pei,‡ GuiXin Liu,‡ WenLu Li,‡ Xiaoman Xiong,‡* Ding Zhou‡* and Na Yao ‡*

Received 16th December 2025
Accepted 23rd January 2026

DOI: 10.1039/d5sc09860b

rsc.li/chemical-science

In acidic systems, elucidating the structural forms and mechanisms of Ru that achieve high activity and stability upon combination with oxides offers valuable insights for designing efficient and durable PEM water electrolysis catalysts. In this study, different Ru forms, including single atoms, sub-nanometric clusters, and heterostructures, were strategically introduced into a WO_x template to systematically investigate their effects on OER performance. *In situ* characterization techniques (ATR-SEIRAS, DEMS, and *in situ* Raman) combined with theoretical calculations reveal that the d–π interactions within the continuously coupled orbitals introduced by subnanometer Ru clusters accelerate electronic delocalization, thereby optimizing the interfacial water structure and hydrogen-bond network and enhancing *OH adsorption. Meanwhile, this interaction facilitates the deprotonation of intermediates, maintains a high surface coverage of *O species, and modulates the post-adsorption electronic structure, which collectively promote *O–*O coupling and the Oxide Path Mechanism (OPM) pathway, endowing the catalyst with superior activity and stability. The resulting Ru_{SNCs}-WO_x exhibits outstanding acidic OER performance, achieving 10 mA cm^{-2} at only 171 mV overpotential and retaining excellent stability over 1000 hours. In PEM electrolyzer tests, it outperforms conventional RuO_2, sustaining 1 A cm^{-2} operation for over 1000 hours.

Introduction

Hydrogen production *via* water electrolysis driven by renewable energy represents a key technology for generating green hydrogen and offers a promising solution to the current energy and environmental challenges. Among the available approaches, proton exchange membrane (PEM) water electrolysis has emerged as a critical driver for advancing the hydrogen economy due to its high efficiency, operational flexibility, and excellent compatibility with renewable energy sources.[1–4] Nevertheless, the commercial viability of PEMWE remains constrained by the sluggish kinetics of the oxygen evolution reaction (OER), which necessitates the use of robust and efficient catalysts.[5,6] While IrO_2 has been widely employed in PEM electrolyzers owing to its exceptional durability, its high cost and the limited supply of Ir pose significant obstacles to large-scale commercialization.[7–9] Consequently, the development of alternative materials that combine high catalytic activity with lower cost has become a major research focus. Among various candidates, Ru-based catalysts stand out due to their relatively low overpotential and outstanding intrinsic activity.[10–12] However, in contrast to IrO_2, the long-term stability of Ru-based catalysts under acidic conditions is poor, which remains a major limitation for their practical application.[13,14]

Currently, in the design of Ru-based catalysts, the introduction of a template is considered an effective strategy.[15–19] For example, Qi *et al.* dispersed Ru single atoms onto a layered manganese dioxide (MnO_2) template to form a Ru–Mn_3O_4 catalyst. This catalyst triggered and regulated the lattice oxygen redox mechanism, achieving a current density of 10 mA cm^{-2} at an overpotential of only 176 mV and maintaining stability for over one year (8800 hours) at 50 mA cm^{-2} [15]. Furthermore, Li *et al.* utilized tantalum-based oxide as a template to construct a RuO_2@TaO_x catalyst with a core–shell structure, which exhibited low overpotentials of 163 and 232 mV at current densities of 10 and 100 mA cm^{-2}, respectively.[18] This approach not only significantly reduces the amount of Ru used, thereby controlling catalyst costs, but also enhances the structural stability of the catalyst and the dispersion of active sites through interactions with the template.[20–23] It has been reported that a small amount of Ru doping can typically be stably anchored within the template, but due to the limited number of active sites the catalytic activity is often insufficient.[24,25] For example, Rong *et al.* reported that atomically dispersed Ru sites on N-doped carbon (Ru_{SAC}/N–C) exhibit lower performance than Ru sites in RuO_x cluster-dispersed systems (Ru_{SAC}@RuO_x/N–C).[26]

State Key Laboratory of New Textile Materials and Advanced Processing, Wuhan. Textile University, Wuhan 430200, P R China. E-mail: yaona@wtu.edu.cn; Dingzhou@whu.edu.cn; 2023021@wtu.edu.cn

† These authors contributed equally to this work.

‡ Present address: No. 1 Sunshine Avenue, Jiangxia District, Wuhan, China.

Conversely, excessive Ru introduction may increase the number of active sites but can lead to particle aggregation and dissolution, causing stability issues and significantly affecting the long-term performance of the catalyst.[27–30] For example, Chen *et al.* reported a heterojunction of ruthenium oxide and zinc-doped cobalt oxide spinel ($RuO_2/ZnCo_2O_4$), which exhibited significantly weaker stability (deactivation after 38.5 h at 10 mA cm^{-2}) compared to the Ru cluster catalyst synthesized on zinc (Zn)-doped cobalt oxide spinel (Ru clusters/$ZnCo_2O_4$), which operated stably for over 700 h at 10 mA cm^{-2}.[31] Therefore, incorporating Ru into the template in a rational form, such that it maintains structural stability while maximizing OER activity, is a central scientific challenge in designing efficient Ru-based catalysts. To date, systematic studies on the relationship between the form of Ru and both OER activity and stability remain limited.[32–35] A deep understanding of the structure–performance relationship of Ru in different forms, along with the elucidation of the underlying mechanisms for enhancing OER performance, is crucial for optimizing catalysts with high activity and durability. Furthermore, this mechanistic insight provides theoretical guidance and design principles for developing cost-effective acidic OER catalytic systems.

Based on these considerations, we strategically introduced Ru in different forms into the WO_x template, including atomically dispersed Ru, subnanometer Ru clusters, and heterostructured RuO_x. Through systematic design and comparative studies of these Ru forms, we seek to elucidate their respective reaction mechanisms during the OER process. Specifically, we aim to clarify the underlying principles that govern how the form of Ru modulates three critical aspects: the distribution of active sites, the interfacial water structure, and the formation and transformation of reaction intermediates. Ultimately, this work serves to establish a scientific foundation for optimization of the catalytic activity and stability in Ru-based catalysts. Combining *in situ* and *ex situ* characterization studies with density functional theory (DFT) calculations, the results indicate that the introduction of subnanometer Ru clusters enhances electronic delocalization *via* d–π interactions within continuously coupled orbitals during the OER process. This effect optimizes the interfacial water structure and hydrogen-bond network within the electric double layer (EDL), accelerates water-splitting kinetics, and increases *OH coverage on the catalyst surface. Moreover, this structure facilitates deprotonation of intermediates and maintains high *O surface coverage, and modulates the post-adsorption electronic structure, thereby promoting *O–*O coupling and the Oxide Path Mechanism (OPM) pathway, resulting in high catalytic activity and excellent stability. Consequently, the synthesized Ru_{SNCs}-WO_x catalyst exhibits an ultralow overpotential of approximately 171 mV to reach 10 mA cm^{-2} in 0.5 M H_2SO_4. Moreover, when employed as the anode catalyst in a proton exchange membrane (PEM) electrolyzer, Ru_{SNCs}-WO_x operates at 1 A cm^{-2} with a cell voltage of only 1.696 V and maintains stable performance even after 1000 hours. This study provides a new theoretical framework and design guidance for the rational design of Ru configurations, aiming to enhance the acid stability and long-term catalytic activity of Ru-based OER catalysts.

Results and discussion

To investigate the effect of Ru species with different sizes on catalytic performance, three types of comparative structures were designed: single atoms (Ru_{SAs}-WO_x), sub-nanometer clusters (Ru_{SNCs}-WO_x), and heterojunctions (RuO_x/WO_x) (Fig. 1a). Among them, the sub-nanometer cluster (Ru_{SNCs}-WO_x) electrocatalyst was synthesized *via* a straightforward two-step method involving rapid thermal annealing (RTA) and hydrothermal treatment. Specifically, WO_x nanosheet templates (WO_x NSs) were prepared by calcining tungstic acid, followed by a hydrothermal reaction with $RuCl_3$ to obtain the target catalyst. The Ru_{SACs}-WO_x single-atom catalyst was prepared by impregnating WO_3 nanosheets with a $RuCl_3$ solution, to achieve a uniform distribution of Ru precursors on the surface, followed by inductively coupled plasma etching (ICP etching) to anchor isolated Ru atoms. The RuO_x/WO_x heterojunction catalyst was synthesized by co-dissolving tungstic acid and $RuCl_3$, mixing thoroughly, and directly calcining the mixture to form a heterointerface between RuO_x and WO_x. The powder X-ray diffraction (XRD) patterns of Ru_{SACs}-WO_x and Ru_{SNCs}-WO_x show the characteristic peaks of hexagonal monoclinic WO_3 (PDF#43-1035), with the main peaks (002), (020), and (200) located at 23.04°, 23.54°, and 24.33°, respectively (Fig. 1b and S1). And the XRD pattern of RuO_x/WO_x exhibits distinct characteristic peaks corresponding to both WO_3 and RuO_2 phases. Based on the observations from transmission electron microscopy (TEM), all three samples are composed of uniformly sized and well-dispersed nanosheets (Fig. S2–4). The high-resolution transmission electron microscopy (HRTEM) image of Ru_{SAs}-WO_x displays well-defined lattice fringes with an interplanar spacing of 0.330 nm, corresponding to the (120) plane of WO_3, which is consistent with the XRD results (Fig. 1c). In the HRTEM image of the Ru_{SNCs}-WO_x sample, similar WO_3 lattice fringes are observed; however, distinct lattice distortions appear in several sub-nanometer regions (Fig. 1d). These distortions are primarily attributed to the incorporation of sub-nanometer Ru clusters, which locally disrupt the WO_3 lattice structure. Furthermore, the HRTEM image shown in Fig. 2g reveals the crystalline coexistence of RuO_2 and WO_3 within the same nanosheet, confirming the successful formation of the RuO_x/WO_x heterostructure (Fig. 1e). Furthermore, individual characterization of the Ru_{SNCs}-WO_x nanosheet sample (Fig. 1f) revealed an interplanar spacing of 0.285 nm, corresponding to the (022) plane of WO_3 (Fig. 1g and h). Further analysis showed that continuous Ru atoms occupied the original W atomic sites, resulting in the formation of the WO_x-like Ru-based phase (Fig. 1i). This structural feature indicates that the sub-nanometer Ru units are not simply supported on the surface of WO_3 but are embedded in the WO_3 lattice through doping or substitution (Fig. 1a). Additionally, scanning transmission electron microscopy-energy dispersive X-ray spectroscopy (STEM-EDS) elemental mapping images reveal a uniform distribution of all elements within Ru_{SNCs}-WO_x (Fig. 1j).

To determine the chemical states of the synthesized catalysts, X-ray photoelectron spectroscopy (XPS) (Fig. S5 and 6) and

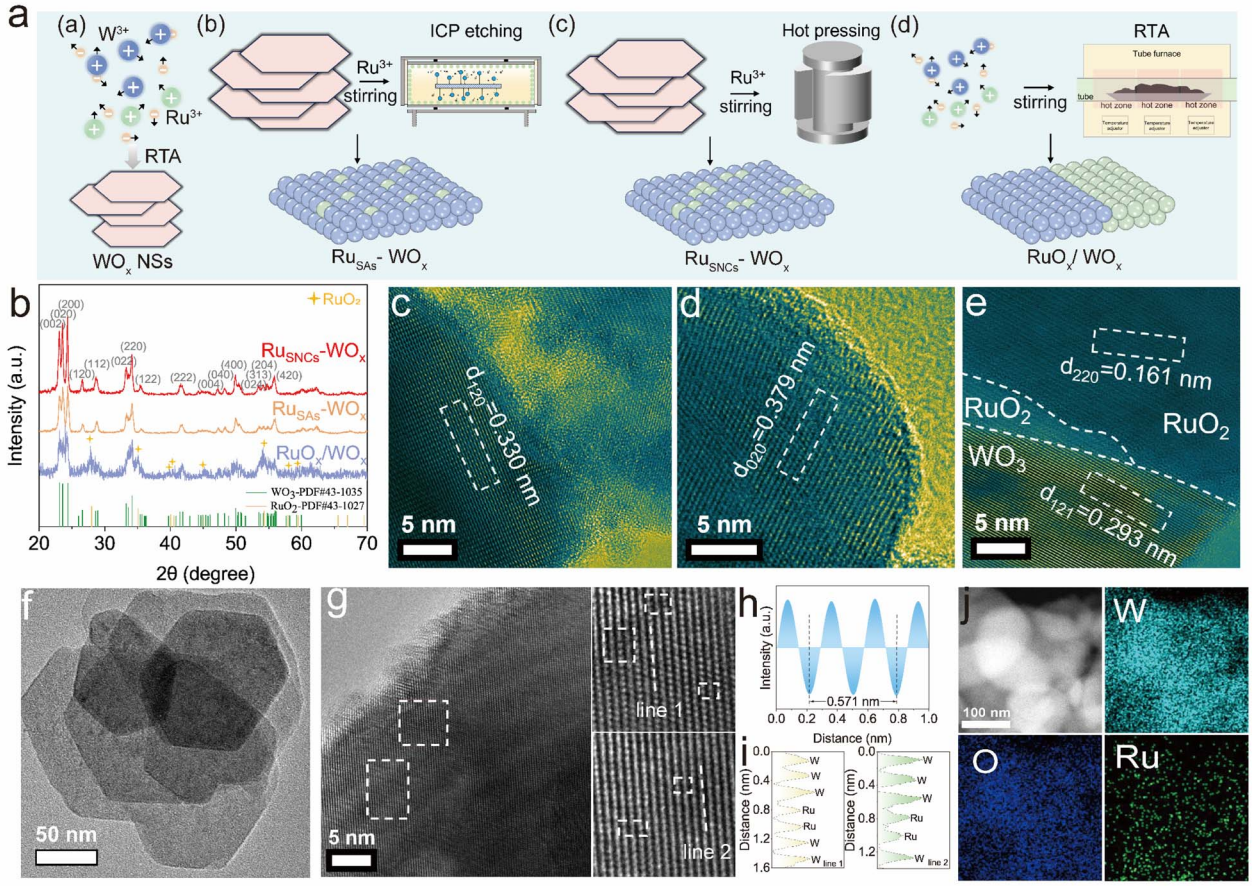

Fig. 1 (a) Schematic illustration of the synthesis of WO_x NSs, single atoms (Ru_{SAs}-WO_x), sub-nanometer clusters (Ru_{SNCs}-WO_x) and hetero-junctions (RuO_x/WO_x). (b) XRD patterns of Ru_{SAs}-WO_x, Ru_{SNCs}-WO_x and RuO_x/WO_x. High-magnification HRTEM images of (c) Ru_{SAs}-WO_x, (d) Ru_{SNCs}-WO_x and (e) RuO_x/WO_x. (f and g) TEM image of Ru_{SNCs}-WO_x and high-magnification HRTEM image of the square regions. (h and i) Lattice rheology profiles of Ru_{SNCs}-WO_x in the square regions in (g). (j) TEM images of elemental distribution of Ru, W, and O in Ru_{SNCs}-WO_x.

X-ray absorption spectroscopy (XAS) were utilized. As shown in Fig. 2a, the W^{6+} peaks corresponding to the W $4f_{7/2}$ binding energy in Ru_{SAs}-WO_x, Ru_{SNCs}-WO_x and RuO_x/WO_x exhibit a negative shift relative to WO_3, indicating electron transfer from Ru species to the W sites. With the increase in Ru content, the electron transfer effect becomes more pronounced. Therefore, the valence state of W is the lowest in RuO_x/WO_x, followed by Ru_{SNCs}-WO_x, and is the highest in Ru_{SAs}-WO_x. However, owing to the distinct electronic interactions between Ru and the WO_x support in different structural configurations, Ru itself displays significantly different valence characteristics (Fig. 2b). Specifically, Ru in Ru_{SNCs}-WO_x exhibits the highest valence state, while Ru in Ru_{SAs}-WO_x shows the lowest, with RuO_x/WO_x lying in between. This finding indicates that the distinct forms of Ru significantly influence the electron transfer behavior between Ru and the substrate. In addition, as shown in the X-ray absorption near-edge structure (XANES) spectra of Ru K-edge (Fig. 2c and d), Ru_{SNCs}-WO_x exhibits a higher absorption edge than Ru_{SAs}-WO_x and RuO_x/WO_x, which is consistent with the conclusions drawn from the XPS analysis. Notably, the Fourier transform extended X-ray absorption fine structure (FT-EXAFS) spectra of Ru K-edge displays two distinct peaks that correspond to the first coordination shell of Ru–O and the second coordination shell of Ru–Ru, respectively (Fig. 2e). The absence of the Ru–Ru peak in Ru_{SAs}-WO_x further confirms the successful construction of isolated Ru single atoms. Furthermore, compared with Ru_{SAs}-WO_x (2.039 Å) and RuO_x/WO_x (2.016 Å), the slightly elongated Ru–O bond length in Ru_{SNCs}-WO_x (2.041 Å) indicates a stronger Ru–O covalency (Fig. 2f, S9, S10, and Table S1). This result is further supported by the wavelet transform (WT) analysis of the EXAFS data (Fig. 2g and S11), demonstrating that the enhanced Ru–O covalent interaction facilitates the adsorption of oxygen intermediates during the acidic OER process.[36–39]

Electrochemical and *in situ* spectroscopic techniques were employed to further investigate the catalytic mechanisms of Ru_{SAs}-WO_x, RuO_x/WO_x, Ru_{SNCs}-WO_x, and RuO_2 reveals the specific contribution of Ru structural effects to the catalytic process. The pH-dependent activity, reflective of the proton transfer decoupled from the electron transfer process, is a hallmark of the lattice oxygen-mediated mechanism (LOM) involving lattice oxygen participation, electrolyte-compensated oxygen vacancies, and chemical deprotonation.[40] As shown in Fig. S12, the LSV curves for Ru_{SAs}-WO_x, RuO_x/WO_x, Ru_{SNCs}-WO_x,

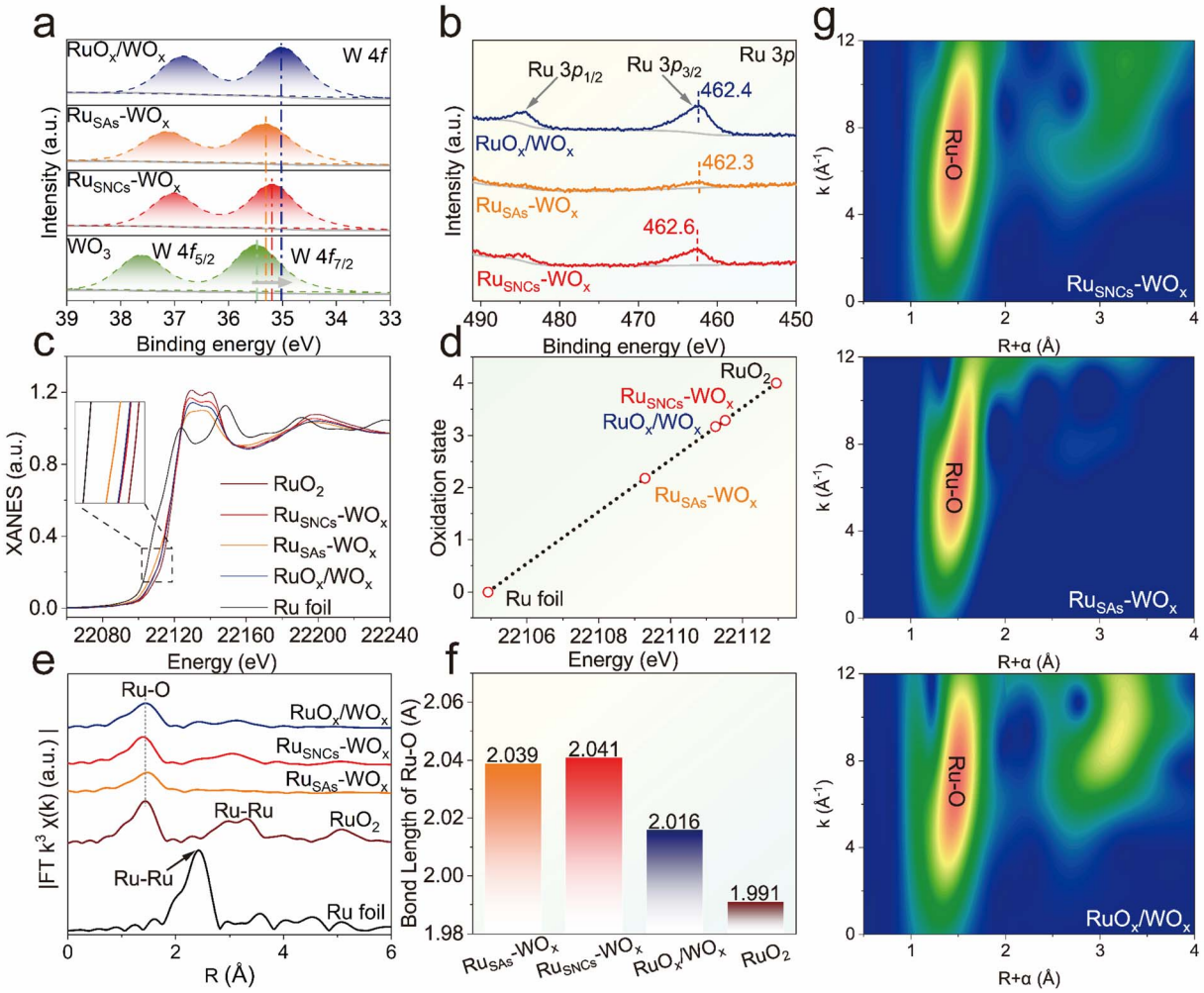

Fig. 2 (a) W 4f core level XPS spectra of Ru_{SAs}-WO_x, Ru_{SNCs}-WO_x, RuO_x/WO_x and WO_3. (b) Ru 3p core level XPS spectra of Ru_{SAs}-WO_x, Ru_{SNCs}-WO_x and RuO_x/WO_x. (c) XANES spectra at the Ru K-edge of Ru_{SAs}-WO_x, Ru_{SNCs}-WO_x, RuO_x/WO_x, Ru foil and RuO_2. (d) Oxidation states of various ruthenium species derived from Ru K-edge XANES. (e) FT-EXAFS of Ru_{SAs}-WO_x, Ru_{SNCs}-WO_x, RuO_x/WO_x, Ru foil and RuO_2. (f) The fitted Ru–M bond length data of Ru_{SAs}-WO_x, Ru_{SNCs}-WO_x, RuO_x/WO_x and RuO_2. (g) Wavelet transform of Ru K-edge EXAFS data of Ru_{SAs}-WO_x, Ru_{SNCs}-WO_x and RuO_x/WO_x.

and RuO_2 in H_2SO_4 solution (pH 0–1) were measured at a scan rate of 5 mV s^{-1}. The Ru_{SAs}-WO_x and Ru_{SNCs}-WO_x samples showed negligible pH dependence on OER kinetics on the RHE scale, providing evidence for the suppression of lattice oxygen participation during the OER process. And RuO_x/WO_x and RuO_2 exhibit significant pH dependence, indicating their OER proceeds *via* the LOM pathway with nonconcerted proton–electron transfer. To further verify the OER pathway, peroxo-like $*O_2^{2-}$ chemical species generated during the LOM were tracked using tetramethylammonium cation (TMA^+), known for its specific interaction with negatively charged species on the catalyst surface and inhibit the LOM cascade (Fig. S13). The RuO_x/WO_x and RuO_2 displayed reduced OER activity and increased Tafel slopes in the presence of TMA^+, indicating the inhibition of the LOM pathway due to strong binding of TMA^+. In contrast, the OER kinetics of Ru_{SAs}-WO_x, Ru_{SNCs}-WO_x, and O remained largely unaffected in the presence of TMA^+, providing further confirmation that Ru_{SAs}-WO_x and Ru_{SNCs}-WO_x effectively suppress the lattice oxygen participation and do not follow the LOM pathway.[41,42] Moreover, due to faster acidic OER kinetics (Tafel slope: 56.41 mV dec^{-1}), better durability, and suppressed lattice oxygen participation, Ru_{SNCs}-WO_x outperforms other samples significantly. Furthermore, *operando* DEMS analysis employing isotope labeling was performed in 0.5 M H_2SO_4 prepared with $H_2{}^{18}O$ to confirm the OER mechanism. For Ru_{SNCs}-WO_x, the mass signals of $^{32}O_2$ ($^{16}O^{16}O$), $^{34}O_2$ ($^{16}O^{18}O$) and $^{36}O_2$ ($^{18}O^{18}O$) were detected (Fig. 3a). It is noteworthy that the appearance of $^{32}O_2$, which results from the direct coupling of two surface-adsorbed ^{16}O species, can be ascribed to the OPM route occurring exclusively on Ru_{SNCs}-WO_x (Fig. 3a). In addition, when the ^{18}O-labeled sample was examined under identical conditions in 0.5 M H_2SO_4 prepared with $H_2{}^{16}O$, the $^{36}O_2$ ($^{18}O^{18}O$) mass signal was still observed, further validating the proposed reaction mechanism (Fig. 3b).[43] Subsequently, *in situ* attenuated total reflection surface-enhanced infrared absorption spectroscopy (ATR-SEIRAS) and *in situ* Raman analysis were

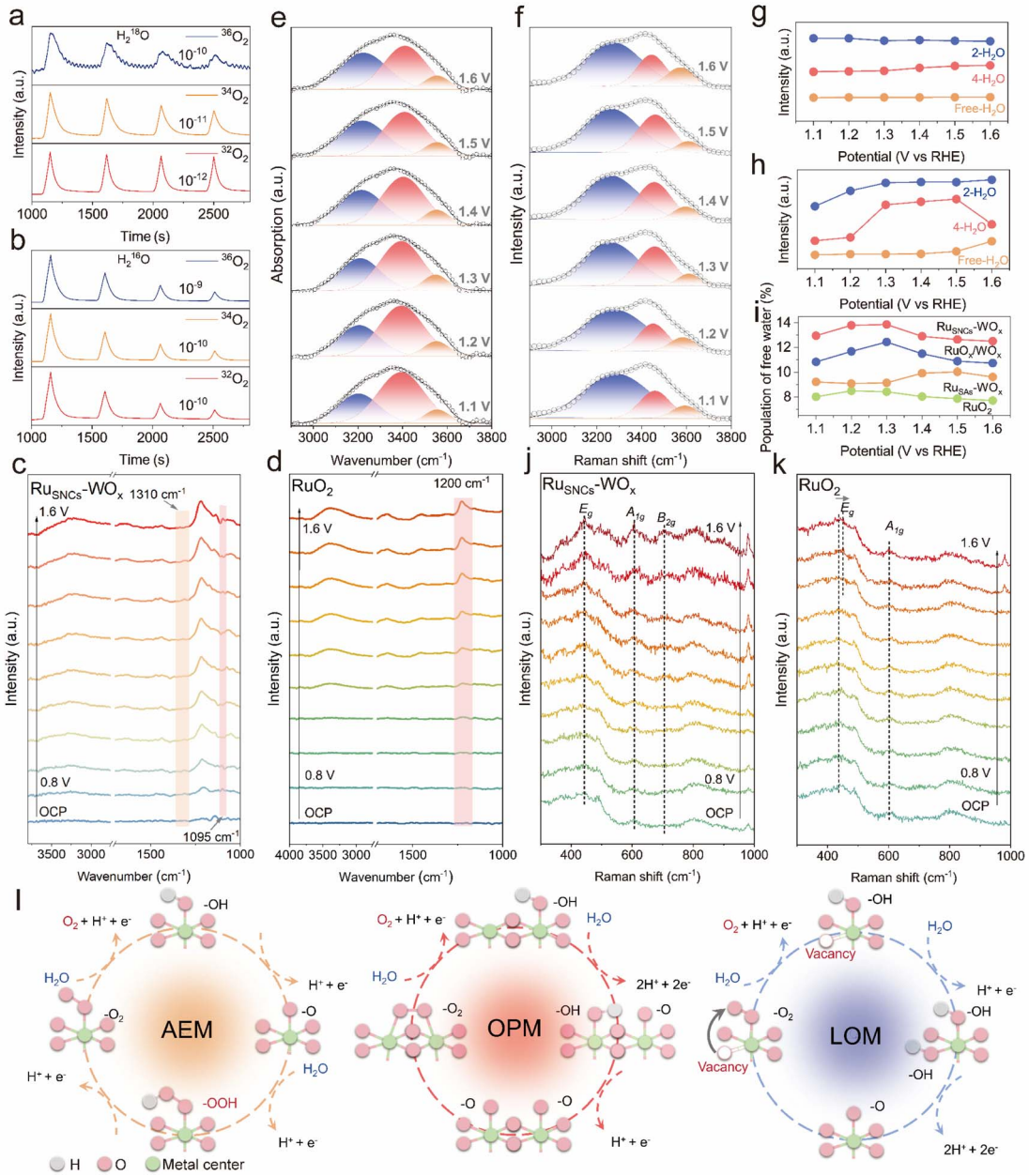

Fig. 3 (a and b) DEMS tests of $^{16}O^{16}O$, $^{18}O^{16}O$ and $^{18}O^{18}O$ signals from the catalysts for ^{18}O-labeled Ru_{SNCs}-WO_x in 0.5 M H_2SO_4 in $H_2{}^{16}O$. (c and d) *In situ* FTIR spectra of the OER on Ru_{SNCs}-WO_x and RuO_2 in 0.5 M H_2SO_4. (e) *In situ* FTIR spectra recorded at potentials from 1.1 V to 1.6 V on Ru_{SNCs}-WO_x. (f) *In situ* Raman spectra recorded at potentials from 1.1 V to 1.6 V on Ru_{SNCs}-WO_x. Percentage of different types of interfacial water structures at applied potentials, as determined by (g) *in situ* FTIR spectra and (h) *in situ* Raman spectra. (i) The proportions of free H_2O at varied potentials of Ru_{SAs}-WO_x, Ru_{SNCs}-WO_x, RuO_x/WO_x, and RuO_2, respectively. (j and k) *In situ* FTIR spectra of the OER on Ru_{SNCs}-WO_x and RuO_2 in 0.5 M H_2SO_4. (l) Simplified schematic diagram of the OER mechanisms for the AEM, LOM, and OPM.

employed to confirm OER mechanisms and elucidate the specific roles of Ru structural effects (Fig. S14 and S15). Fig. 3c shows the emergence of distinctive vibration frequencies at 1095 cm^{-1} and 1310 cm^{-1} with the applied potential gradually increasing from 1.3 to 1.5 V in Ru_{SNCs}-WO_x. Based on previous reports, the emergence of vibration bands at approximately 1100 and 1300 cm^{-1} can be assigned to the bridging oxygen configuration at the dual active site.[44–46] This potential-dependent SR-FTIR absorption band indicates that the key *O–O* intermediate emerges at the dual-metal active sites simultaneously, forming a characteristic M–*O–O*–M configuration, suggesting that Ru_{SNCs}-WO_x follows an OPM pathway. In contrast, a distinct potential-dependent peak in RuO_x/WO_x and RuO_2 emerges at ~1200 cm^{-1}, which are attributed to the stretching vibrations of the *OO intermediate, confirming the reaction pathway of the LOM route (Fig. 3d and S16).[22,47] On Ru_{SAs}-WO_x, only the *OOH intermediate (~1050 cm^{-1}) corresponding to the AEM pathway is detected, further supporting

that the low covalency of Ru–O in Ru_{SAs}-WO_x fails to activate the lattice oxygen.[15]

In acidic electrolytes, the OER mechanisms of AEM, LOM, and OPM all rely on *OH compensation, making water dissociation a critical factor due to the inherently low OH^- concentration.[41,48–54] The hydrogen-bond network in electrical double-layers governs water adsorption/dissociation and proton transfer for the acidic OER. Thus, precisely controlling interfacial water availability and activity is a vital strategy to improve the OER performance. The Raman peaks located at ~3200, ~3400, and ~3600 cm^{-1} were attributed to 4-coordinated hydrogen-bonded water (4-HB H_2O), 2-coordinated hydrogen-bonded water (2-HB-H_2O), and free H_2O, respectively. As shown in Fig. 3e, g and S17–19, 2-HB-H_2O is the predominant species at all detected potentials in all catalysts, ensuring effective proton transfer during the acidic OER process.[55–57] With increasing voltage, the proportion of free H_2O increases progressively in all Ru-based-WO_x samples, most significantly in Ru_{SNCs}-WO_x, followed by Ru_{SAs}-WO_x and RuO_x/WO_x, while RuO_2 exhibits a reverse trend (Fig. 3i). This behavior is attributed to the Ru–W interaction and sub-nanometer Ru size, which enhance hydrogen-bond regulation and modulate the electronic environment of interfacial water. Consequently, bound water dynamically converts to active free water, sustaining interfacial reactions by replenishing water consumed during the acidic OER.[12] This result was further validated by *in situ* Raman spectroscopy (Fig. 3f, h and S17–19). We further employed rotating ring-disk electrode (RRDE) measurements (see the Methods section in the SI) to perform *in situ* monitoring of the local pH at the disk electrode. We observed that the initial local pH values of the Ru_{SNCs}-WO_x, Ru_{SAs}-WO_x, and RuO_x/WO_x electrodes were identical and comparable to that of the bulk solution. Furthermore, when the potential reached the onset potential for the oxygen evolution reaction (OER) (1.4 V *vs.* RHE for Ru_{SNCs}-WO_x and 1.45 V *vs.* RHE for Ru_{SAs}-WO_x and RuO_x/WO_x), the local pH of the catalysts changed due to the generation of protons at the interface during the OER process, as illustrated in Fig. S20–S22. More notably, given that the OER is a proton-coupled electron transfer (PCET) process, Ru_{SNCs}-WO_x exhibited both accelerated deprotonation kinetics and a smaller variation trend in the interfacial local pH, as shown in Fig. S23(b). Specifically, at the same potential (*e.g.*, 1.75 V *vs.* RHE), Ru_{SNCs}-WO_x delivered a higher OER current density than Ru_{SAs}-WO_x and RuO_x/WO_x, accompanied by an enhanced local pH. This collectively indicates that the deprotonation capability at the Ru_{SNCs}-WO_x interface is strengthened. In addition, the correlation between the local pH and current density in Fig. S23(c) reveals that the pH variation of Ru_{SNCs}-WO_x was negligible compared to that of Ru_{SAs}-WO_x and RuO_x/WO_x. This implies that Ru_{SNCs}-WO_x does not suffer from proton accumulation at the interface, providing compelling evidence for the enhanced proton flux at the Ru_{SNCs}–WO_x interface.[58,59] Moreover, the *in situ* Raman spectra in Fig. 3j, k and S24 reveal characteristic signals at approximately ~450 cm^{-1}, ~510 cm^{-1}, and ~700 cm^{-1}, corresponding to the E_g, A_{1g}, and B_{2g} modes of RuO_2, respectively.[30] As the potential increases, the E_g and A_{1g} peaks of Ru_{SNCs}-WO_x show a marked enhancement, attributed to the increased Ru–O bonding caused by intermediate adsorption during the OPM process. Conversely, this enhancement in Ru_{SAs}-WO_x is less evident and requires higher potentials, indicating faster reaction kinetics along the OPM pathway of Ru_{SNCs}-WO_x. Notably, unlike in RuO_x/WO_x and RuO_2, no blue shift of the E_g and A_{1g} peaks in Ru_{SNCs}-WO_x is observed, where the blue shift arises from the elongation of Ru–O bonds caused by the formation of oxygen vacancy intermediates during the LOM process, which confirm that Ru_{SNCs}-WO_x does not follow the LOM path. Notably, the continuous intensity enhancement of the asymmetric B_{2g} mode Raman peak in Ru_{SNCs}-WO_x with increasing potential, which is not prominent in other Ru samples, provides additional evidence for the rapid compensation of *OH in Ru_{SNCs}-WO_x. Based on the above analysis, the sub-nanocluster effect can alter the OER mechanism and significantly modulate the electronic environment of water molecules (*i.e.* promoting the transition of interfacial water from a bound state to a more reactive free state). This transition contributes to improved reaction kinetics for the OER, facilitates more efficient water dissociation and increases the generation rate of *OH intermediates at Ru sites, thereby enhancing the dynamic replenishment of intermediates during the OPM process and ultimately improving the catalytic activity and stability of Ru-based catalysts (Fig. 3l).

The acidic OER performance of the prepared catalysts was evaluated in 0.5 M H_2SO_4 electrolyte using a standard three-electrode system. As shown in the linear sweep voltammetry (LSV) curves in Fig. 4a, Ru_{SNCs}-WO_x exhibits superior OER activity compared with other samples. To achieve a current density of 10 mA cm^{-2}, Ru_{SNCs}-WO_x requires an overpotential of 171 ± 1 mV, which is significantly lower than those of Ru_{SAs}-WO_x (207 ± 1 mV), RuO_x/WO_x (208 ± 1 mV), and RuO_2 (240 ± 1 mV) (Fig. 4b). Furthermore, the reaction kinetics of all samples were evaluated from the Tafel slopes derived from the polarization curves, as shown in Fig. 4c. Ru_{SNCs}-WO_x exhibits a Tafel slope of 56.41 mV dec^{-1}, which is lower than those of Ru_{SAs}-WO_x (110.66 mV dec^{-1}), RuO_x/WO_x (71.04 mV dec^{-1}), and RuO_2 (132.89 mV dec^{-1}), indicating its superior electrochemical kinetics. The smaller charge transfer resistance (R_{ct}) of Ru_{SNCs}-WO_x at 1.5 V *vs.* RHE, as measured by *in situ* electrochemical impedance spectroscopy (EIS), further supports this conclusion (Fig. S25). Combined with the analysis of the Bode phase plots, although Ru_{SNCs}-WO_x exhibits behavior similar to other catalysts in terms of the low phase angles in the high-frequency region (corresponding to the electron transfer response within the catalyst layer), its high phase angles in the low-frequency region (corresponding to the electron transfer response at the catalyst–electrolyte interface) decrease more rapidly with increasing potential (Fig. 4d, e and S26). This observation indicates an accelerated electron transfer response at the Ru_{SNCs}-WO_x catalyst–electrolyte interface, which facilitates more efficient reaction kinetics and thereby enhances the OER activity.[38,60] To further evaluate the intrinsic activity of Ru_{SNCs}-WO_x, its turnover frequency (TOF) and electrochemical active surface area (ECSA) were calculated. Notably, at 1.55 V *vs.* RHE, Ru_{SNCs}-WO_x exhibits the highest TOF value of 0.202 s^{-1}, which is 5.19 times that of RuO_2 (0.039 h^{-1}), indicating its markedly

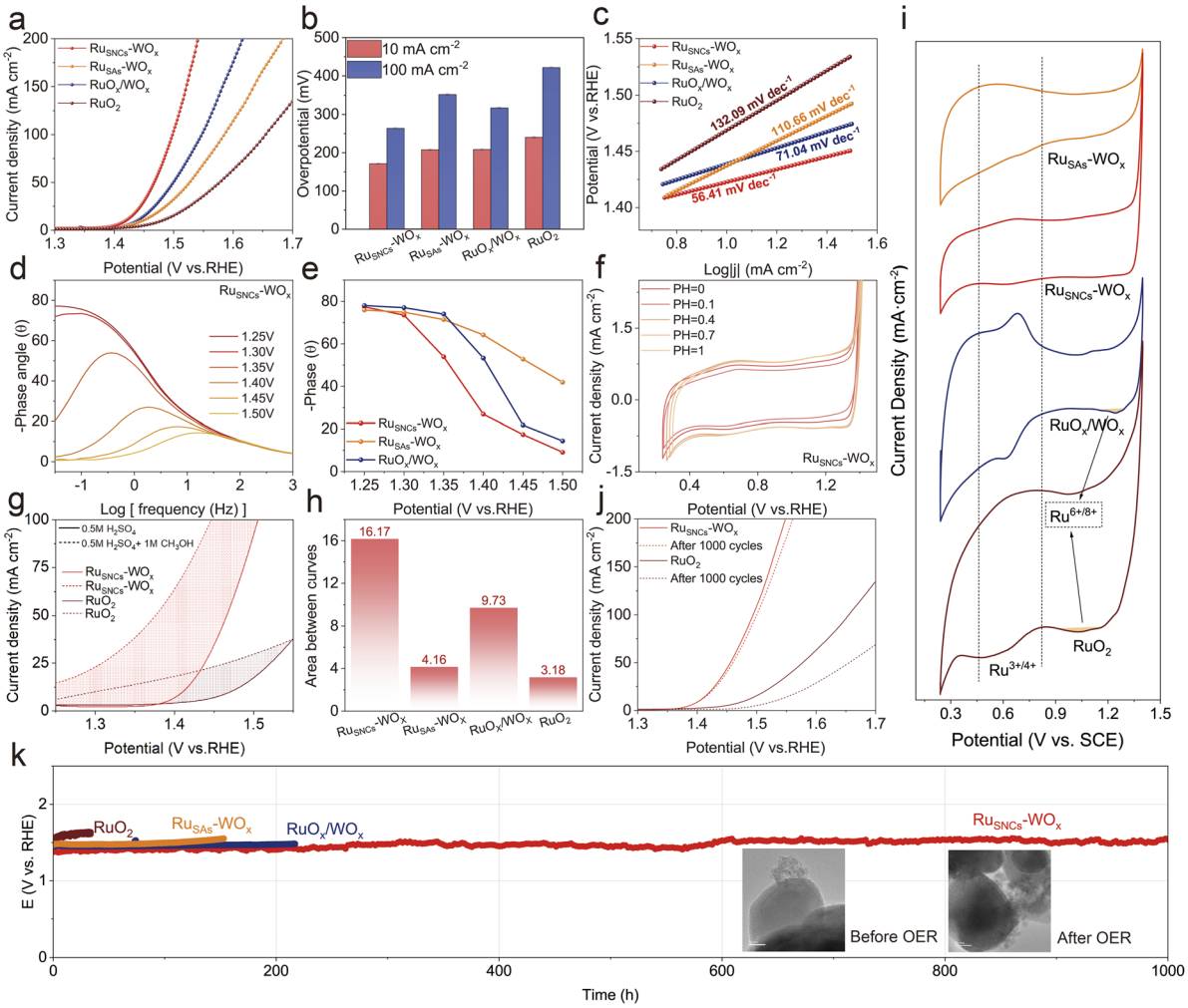

Fig. 4 (a) LSV curves of Ru_{SAs}-WO_x, Ru_{SNCs}-WO_x, RuO_x/WO_x and RuO_2 in 0.5 M H_2SO_4 solution. (b) Comparison of overpotentials at a current density of 10 mA cm^{-2} and 100 mA cm^{-2}. (c) Corresponding Tafel plots according to the LSV curves in (a). (d) Bode phase plots of Ru_{SNCs}-WO_x at different voltages. (e) Summarized phase peak angles of Ru_{SAs}-WO_x, Ru_{SNCs}-WO_x, RuO_x/WO_x and RuO_2 at 1.25-1.50 V. (f) pH independent CV analysis of redox peaks of Ru_{SNCs}-WO_x measured from 0.0 to 1.4 V *vs.* SCE. (g) LSV curves of Ru_{SNCs}-WO_x recorded with and without 1 M methanol. (h) The enclosed area between the integrated corresponding polarization curves of (g). (i) CV analysis of redox peaks of Ru_{SAs}-WO_x, Ru_{SNCs}-WO_x, RuO_x/WO_x and RuO_2 measured from 0.0 to 1.4 V *vs.* SCE. (j) LSV curves of initial and after 1000 CV cycles on Ru_{SNCs}-WO_x. (k) The chronopotentiometric curves of Ru_{SAs}-WO_x, Ru_{SNCs}-WO_x, RuO_x/WO_x, and RuO_2, alongside the TEM images of Ru_{SNCs}-WO_x recorded before and after the OER test, where the chronopotentiometric curves were all acquired at a constant current density of 10 mA cm^{-2}.

enhanced intrinsic OER activity (Fig. S27). The double-layer capacitance (C_{dl}) is a key parameter for estimating the ECSA and was experimentally determined to assess the intrinsic catalytic activity (Fig. S28). As shown in Fig. S29, the C_{dl} value of Ru_{SNCs}-WO_x was measured to be 39.2 mF cm^{-2}, surpassing those of Ru_{SAs}-WO_x (14.4 mF cm^{-2}) and RuO_x/WO_x (36.2 mF cm^{-2}), indicating a greater number of active surface sites for the OER process. Furthermore, the ECSA-normalized OER activity of Ru_{SNCs}-WO_x consistently outperforms those of Ru_{SAs}-WO_x, RuO_x/WO_x, and RuO_2, confirming its outstanding intrinsic acidic OER activity (Fig. S30). In addition, as the electrolyte pH increases, the H_2 desorption potential of Ru_{SNCs}-WO_x shifts markedly in the positive direction (Fig. 4f and S31). This suggests that the incorporation of Ru sub-nanoclusters significantly enhances the catalyst's ability to promote water dissociation, thereby increasing the surface coverage of *OH species. Subsequently, methanol was employed as a molecular probe to assess the surface coverage of *OH species, as the methanol oxidation reaction (MOR) proceeds *via* nucleophilic attack of methanol molecules on electrophilic *OH groups. Upon introducing 1.0 M methanol into 0.5 M H_2SO_4 solution, all samples and RuO_2 exhibited a pronounced increase in current density, attributable to methanol electro-oxidation (Fig. 4g and S32). The difference in current density induced by the MOR was quantified by integrating the enclosed area between the corresponding polarization curves, since this area is directly proportional to the amount of charge transferred. Compared with Ru_{SAs}-WO_x, RuO_x/WO_x, and RuO_2, Ru_{SNCs}-WO_x displayed a larger current difference between the MOR and OER (Fig. 4h), indicating a stronger *OH replenishment capability, which in turn contributes to its enhanced OER activity and stability. Cyclic voltammetry (CV) measurements were performed at a scan rate

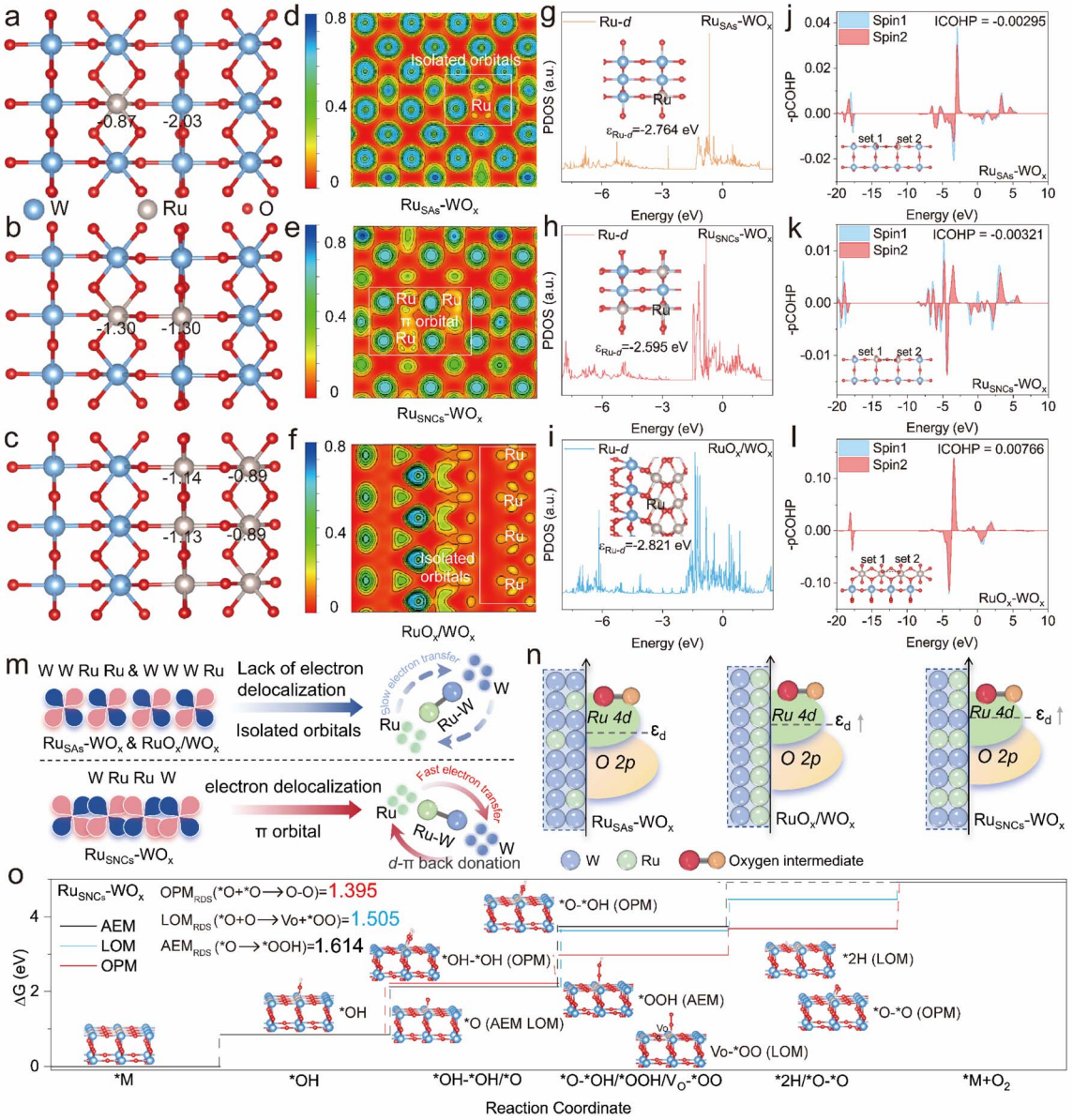

Fig. 5 (a–c) Charge transfer behavior of Ru_{SAs}-WO_x, Ru_{SNCs}-WO_x, and RuO_x/WO_x. (d–f) The ELF graphs for Ru_{SAs}-WO_x, Ru_{SNCs}-WO_x, and RuO_x/WO_x. (g–i) DOS plots of Ru 4d states in Ru_{SAs}-WO_x, Ru_{SNCs}-WO_x, and RuO_x/WO_x. (j–l) Crystal Orbital Hamiltonian Population of Ru_{SAs}-WO_x, Ru_{SNCs}-WO_x, and RuO_x/WO_x. (m) Schematic diagram of the influence of d-band coupling on the electron transfer rate of ruthenium sites in Ru_{SAs}-WO_x, Ru_{SNCs}-WO_x, and RuO_x/WO_x during the oxygen reduction reaction. (n) Schematic diagram of Ru 4d and O 2p orbitals in Ru_{SAs}-WO_x, Ru_{SNCs}-WO_x and RuO_x/WO_x. (o) Illustration of Gibbs free energy of Ru_{SNCs}-WO_x catalysts during the OER process by AEM, LOM and OPM pathways.

of 5 mV s^{-1} to investigate the oxidation behavior of Ru sites at high potentials in Ru-based-WO_x and RuO_2. For RuO_x/WO_x and RuO_2, three distinct redox peaks were observed at approximately 0.64, 1.03, and 1.12 V, corresponding to the Ru^{3+}/Ru^{4+}, Ru^{4+}/Ru^{6+}, and Ru^{6+}/Ru^{8+} transitions, respectively.[61–63] In contrast, the Ru_{SNCs}-WO_x sample showed no detectable peaks associated with the Ru^{4+}/Ru^{6+} and Ru^{6+}/Ru^{8+} transitions (Fig. 4i), indicating that Ru sub-nanoclusters can suppress the electron-donating behavior of Ru, thereby inhibiting the formation of high-valent Ru^{n+} (n >4) species and enhancing the OER stability. The long-term operational stability of Ru_{SNCs}-WO_x under acidic conditions was further confirmed by chronoamperometric stability testing and extended CV cycling. The long-term operational stability of Ru_{SNCs}-WO_x under acidic conditions was further evaluated by chronoamperometric stability testing and extended CV cycling. As expected, the LSV curves of Ru_{SNCs}-WO_x exhibited negligible degradation after 1000 CV cycles, whereas the overpotential of RuO_2 increased significantly (Fig. 4j). Stability was also assessed *via* chronoamperometric measurements at a current density of 10 mA cm^{-2}, revealing that Ru_{SNCs}-WO_x maintained a steady operation for over 1000 h, while RuO_2 and other samples experienced

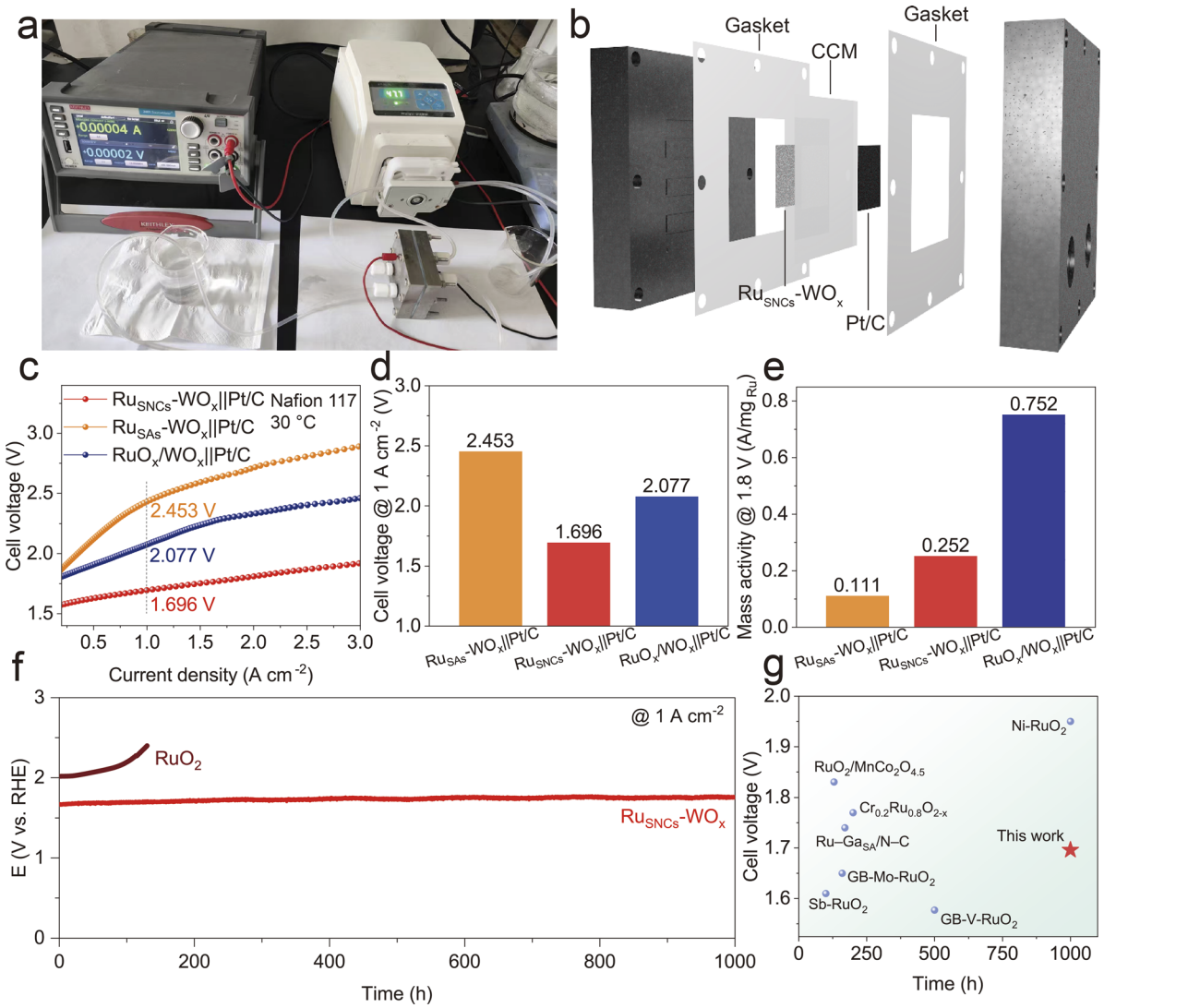

Fig. 6 (a) PEMWE device. (b) Schematic of the PEMWE cell. (c) The polarization curves of PEMWE obtained using Ru$_{SAs}$WO$_x$, Ru$_{SNCs}$-WO$_x$, and RuO$_x$/WO$_x$ as the anode catalysts at 30 °C with a Nafion 117 proton exchange membrane. (d) Comparison of overpotentials for Ru$_{SNCs}$-WO$_x$||Pt/C, Ru$_{SAs}$-WO$_x$||Pt/C and RuO$_x$/WO$_x$||Pt/C at a current density of 1 A cm^{-2}. (e) Mass activity of Ru$_{SNCs}$-WO$_x$||Pt/C, Ru$_{SAs}$-WO$_x$||Pt/C and RuO$_x$/WO$_x$||Pt/C based on the mass of Ru. (f) Chronopotentiometry of PEMWE based on Ru$_{SNCs}$-WO$_x$||Pt/C and RuO$_2$||Pt/C. (g) Comparison of the stability of PEMWE using Ru$_{SNCs}$-WO$_x$ as well as other reported RuO$_2$-based anode catalysts.

rapid performance decay under identical conditions (Fig. 4k). Compared with recently reported Ru-based catalysts, Ru$_{SNCs}$-WO$_x$ demonstrated improved activity and durability, outperforming most state-of-the-art Ru-based catalysts to date (Table S2). Additionally, post-OER XPS and XRD analyses confirmed the excellent structural stability of Ru$_{SNCs}$-WO$_x$, with spectra remaining consistent with those recorded prior to OER testing (Fig. S33 and S34). The TEM images in Fig. 4K, recorded before and after the OER stability test, demonstrate that the morphology of Ru$_{SNCs}$-WO$_x$ remains unaltered following stability evaluation.

To elucidate the fundamental reasons Ru$_{SNCs}$-WO$_x$ exhibits superior activity and stability compared to Ru$_{SAs}$-WO$_x$ and RuO$_x$/WO$_x$, we performed density functional theory (DFT) calculations to analyze the local electronic environment of Ru$_{SNCs}$-WO$_x$ (for additional computational details, please refer to the Methods section and the computational model illustrated in Fig. S35). We performed Bader charge analysis to investigate the surface charge distribution of Ru$_{SNCs}$-WO$_x$, Ru$_{SAs}$-WO$_x$, and RuO$_x$/WO$_x$. As shown in Fig. 5a–c, the Ru species in Ru$_{SNCs}$-WO$_x$ exhibit the highest oxidation state, which is consistent with the XPS and XAS results. This elevated oxidation state facilitates the adsorption of *OH and *O intermediates on the Ru sites of Ru$_{SNCs}$-WO$_x$.[64,65] In addition, the electron localization function (ELF) was calculated. As shown in Fig. 6d–f and S36, a laterally overlapped coupled orbital (*i.e.*, an extended π orbital) is formed between the sub-nanometer Ru clusters and W in Ru$_{SNCs}$-WO$_x$, which facilitates electron delocalization through d–π interactions. In contrast, the coupling orbitals between Ru and W in Ru$_{SAs}$-WO$_x$ and RuO$_x$/WO$_x$ remain relatively separated,

hindering electron transfer between them and resulting in a significantly lower Ru valence state in these two structures compared with Ru_{SNCs}-WO_x. The π orbital effect between W and Ru_{SNCs} in Ru_{SNCs}-WO_x reduces the positive charge on the surface of the stably existing H_3O^+ ions in solution, thereby disrupting their stability and causing their decomposition (loss of one H^+) into free water molecules (H_2O). By observing the changes in the solvation structure (the arrangement of water molecules around the W/Ru sites) (Fig. S37 and S38), the occurrence of this transformation can be clearly seen, thereby confirming the aforementioned effect. Meanwhile, this accelerates the dissociation of H_2O and thereby enhances the supply of *OH, as evidenced by the differential charge analysis (Fig. S39). In addition, the partial density of states (PDOS) analysis reveals that the introduction of Ru sub-nanoclusters upshifts the *d*-band center of Ru (Fig. 5g–i), thereby strengthening the covalency of Ru and enhancing its adsorption capability toward oxygen intermediates at the Ru sites (Fig. 5n).[66] I in addition, due to the limited electronic delocalization in the single-atom system and the heterojunction, the change in the valence state of adjacent W atoms is minimal when *OH is adsorbed on the Ru sites in Ru_{SAs}-WO_x and RuO_x-WO_x (Fig. S40a and b). In contrast, in the sub-nanostructured Ru_{SNCs}-WO_x, the electron delocalization effect enables *OH adsorption at the Ru site to markedly enhance the electron-donating capability of W atoms (Fig. S40c and d), thereby facilitating the adsorption of another *OH at the W site. Moreover, this electron delocalization effect also enhances the polarization of *OH (Fig. S41), thereby promoting its deprotonation to form *O. Moreover, as shown in Fig. S42, the O*–Ru–*O bond angle and bond length on the surface of Ru_{SNCs}-WO_x decrease to 89.53° and 1.62 Å, respectively, compared with 90.43° and 1.73 Å in Ru_{SAs}-WO_x and 95.14° and 1.80 Å in RuO_x/WO_x. This indicates that the lattice confinement effect in Ru_{SNCs}-WO_x is disrupted, resulting in a shortened *O–*O distance and optimized bond angle, thereby facilitating *O–*O coupling (as evidenced by the smaller COHP value of Ru_{SNCs}-WO_x) (Fig. 5j–l), which in turn favors the OPM pathway.[46] Moreover, we calculated the Gibbs free energy changes of Ru_{SNCs}-WO_x, Ru_{SAs}-WO_x and RuO_x/WO_x during the OER *via* the AEM, LOM, and OPM pathways. As expected, Ru_{SNCs}-WO_x exhibits the lowest energy barrier for the rate-determining step (~1.395 eV) through the OPM pathway (Fig. 5o and S43). Based on the above discussion, the improvement in the OER performance of the Ru_{SNCs}-WO_x catalyst arises from two main aspects: (i) the incorporation of Ru sub-nanoparticles facilitates the transformation of the stable H_3O^+ configuration in acidic media into free water molecules, which accelerates water dissociation, increases the availability of *OH intermediates, and thereby enhances the kinetics of the OPM pathway. (ii) It promotes intermediate deprotonation and strengthens *OO coupling, effectively reducing the energy barrier of the rate-determining step in the OPM pathway, thus markedly improving the catalytic activity.

Inspired by the excellent overall activity and stability of Ru_{SNCs}-WO_x in the OER, we selected Ru_{SNCs}-WO_x as the anode catalyst (loading: 2 mg cm^{-2}) for the OER and commercial Pt/C as the cathode catalyst (loading: 1 mg cm^{-2}) for the hydrogen evolution reaction (HER) and used a proton exchange membrane (Nafion 117) to fabricate a membrane electrode assembly (MEA) to evaluate its performance in an actual proton exchange membrane water electrolysis (PEMWE) cell (Fig. 6a and b). All device performance evaluations were conducted in deionized water at 80 °C. As shown in Fig. 6c, the Ru_{SNCs}-WO_x‖Pt/C membrane electrode assembly achieved a water electrolysis current density of 1.0 A cm^{-2} and 2.0 A cm^{-2} at cell voltages of only 1.696 V and 1.810 V, which are significantly lower than those of the Ru_{SAs}-WO_x‖Pt/C and RuO_x/WO_x‖Pt/C membrane electrode assembly and superior to most reported Ru-based catalysts (Fig. 6g and Table S3). In addition, the Ru_{SNCs}-WO_x‖Pt/C membrane electrode assembly reliably operated for 1000 hours at a current density of 1 A cm^{-2} (Fig. 6d), significantly outperforming the other catalysts. Significantly, as shown in the SEM images of Ru_{SNCs}-WO_x‖Pt/C before and after the stability test, the distribution of the catalyst on the membrane surface and the microscopic surface morphology (such as wrinkling) have not changed significantly (Fig. S44), further confirming the durability and structural integrity of the MEA during the PEMWE testing. The Ru_{SNCs}-WO_x catalyst demonstrated outstanding device performance, proving its great potential for future hydrogen production applications.

Conclusion

In summary, we reveal the significant effect of structural forms. By comparing systems of Ru single atoms, Ru sub-nanoclusters, and heterostructured Ru incorporated into WO_x nanosheets, we systematically investigated the impact of structural forms on catalytic performance. Combined with various *in situ* characterization techniques and theoretical calculations, we found that: on one hand, the introduction of Ru sub-nanoclusters regulates the interfacial water structure, which accelerates water dissociation and ensures continuous generation of *OH. On the other hand, the electron delocalization effect of the Ru sub-nanocluster systems accelerates deprotonation of intermediates and then maintains a high surface coverage of *O and promotes *O–*O coupling, thereby enhancing OPM kinetics. Owing to this unique subnanocluster regulation strategy, Ru_{SNCs}-WO_x not only effectively facilitates the OPM pathway but also markedly enhances OPM kinetics, thereby boosting the OER performance of Ru-based catalysts. This catalyst exhibits outstanding OER performance under acidic conditions, achieving a current density of 10 mA cm^{-2} at an overpotential of only 171 mV and maintains excellent durability with almost no performance decay over 1000 hours. Moreover, Ru_{SNCs}-WO_x‖Pt/C demonstrates exceptional performance in a PEM electrolyzer, achieving stable operation at 1 A cm^{-2} under a low cell voltage of only 1.696 V for over 1000 hours. This work systematically elucidates the critical impact of size effects on the OER, providing rational design principles for high-efficiency Ru-based catalysts for the OPM pathway and laying a solid foundation for developing highly efficient catalytic systems for large-scale green hydrogen production. The d–π interaction can similarly modulate interfacial reactant adsorption (*e.g.*, H_2O, O_2, CO_2, *etc.*) and intermediate transformation. By optimizing

the size of metal clusters and the electronic structure of oxide templates, this strategy can be extended to design highly efficient and durable catalysts for various electrocatalytic reactions, establishing a universal design principle that bridges structural configurations and catalytic performance.

Author contributions

Conceptualization: X. X., D. Z., and N. Y. Methodology: X. Z., A. C., J. P., G. L., W. L., X. X., D. Z. and N. Y. Investigation: X. Z., X. X., D. Z. and N. Y. Visualization: X. Z., A. C., J. P., G. L., and W. L. Supervision: X. X., D. Z. and N. Y. Writing – original draft: A. C., J. P., G. L., W. L., X. X., D. Z. and N. Y. Writing – review and editing: X. Z., D. Z., X. X. and N. Y.

Conflicts of interest

The authors declare no conflict of interest.

Data availability

Supplementary information (SI) is available. See DOI: https://doi.org/10.1039/d5sc09860b.

Acknowledgements

This work was financially supported by the National Natural Science Foundation of China (No. 22309137), Department of Science and Technology of Hubei Province (2024CSA076), Natural Science Foundation of Hubei Province (2025AFB860), and Youth Talent Project of Scientific Research Program funded by the Hubei Provincial Department of Education (Q20231704). We acknowledge the great help from Prof. Weilin Xu and co-workers at Wuhan Textile University for helpful measurements and discussion. We thank the Analytical and Testing Center of Wuhan Textile University for XRD and Raman testing.

References

1 M. Carmo, D. L. Fritz, J. Mergel and D. Stolten, *Int. J. Hydrogen Energy*, 2013, **38**, 4901–4934.
2 Z. o. Yu, Y. Duan, X. u. Feng, X. Yu and S. Yu, *Adv. Mater.*, 2021, **33**, 200710.
3 L. Chong, G. Gao, J. Wen, H. Li, H. Xu, Z. Green, J. D. Sugar, A. J. Kropf, W. Xu, X.-M. Lin, H. Xu, L. Wang and D.-J. Liu, *Science*, 2023, **380**, 609–616.
4 C. Wei, C. Liu, Z. Zhang, K. Sun, C. Xing, W. Shi, Y. Li, J.-F. Li and B. Zhang, *Joule*, 2025, **9**, 102058.
5 C. Spoeri, J. T. H. Kwan, A. Bonakdarpour, D. P. Wilkinson and P. Strasser, *Angew. Chem., Int. Ed.*, 2017, **56**, 5994–6021.
6 C. C. L. McCrory, S. Jung, I. M. Ferrer, S. M. Chatman, J. C. Peters and T. F. Jaramillo, *J. Am. Chem. Soc.*, 2015, **137**, 4347–4357.
7 C. Minke, M. Suermann, B. Bensmann and R. Hanke-Rauschenbach, *Int. J. Hydrogen Energy*, 2021, **46**, 23581–23590.
8 M. Clapp, C. M. Zalitis and M. Ryan, *Catal. Today*, 2023, **420**, 114140.
9 J. Chen, Y. Ma, C. Cheng, T. Huang, R. Luo, J. Xu, X. Wang, T. Jiang, H. Liu, S. Liu, T. Huang, L. Zhang and W. Chen, *J. Am. Chem. Soc.*, 2025, **147**, 8720–8731.
10 S. Cherevko, A. R. Zeradjanin, A. A. Topalov, N. Kulyk, I. Katsounaros and K. J. J. Mayrhofer, *Chem Catal.*, 2014, **6**, 114140.
11 Z. W. Seh, J. Kibsgaard, C. F. Dickens, I. B. Chorkendorff, J. K. Norskov and T. F. Jaramillo, *Science*, 2017, **355**, eaad4998.
12 J. Li, H. Cheng, Y. Sun, R. Ma, D. Li, Y. Xu, J. Jin, X. Liu, M. Shao and L. Wang, *Nat. Mater.*, 2025, DOI: 10.1038/s41563-025-02405-5.
13 Q. Wang, Y. Cheng, H. B. Tao, Y. Liu, X. Ma, D.-S. Li and H. B. Yang, *Angew. Chem., Int. Ed.*, 2023, **62**, e202216645.
14 L. Hou, X. Gu, X. Cui, J. Tang, Z. Li, X. Liu and J. Cho, *EES Catal.*, 2023, **1**, 619–644.
15 M. Qi, X. Du, X. Shi, S. Wang, B. Lu, J. Chen, S. Mao, H. Zhang and Y. Wang, *J. Am. Chem. Soc.*, 2025, **147**, 18295–18306.
16 H. Jia, N. Yao, Y. Jin, L. Wu, J. Zhu and W. Luo, *Nat. Commun.*, 2024, **15**, 5419.
17 J. Li, Y. Zhu, C. Li, Q. Zhang, J. Rong, S. Guo, N. Alonso-Vante, L. Yang, M.-H. Yeh, W.-H. Huang, X. Yu, H. Cheng and J. Ma, *Nat. Commun.*, 2025, **16**, 8827.
18 J. Li, X. Yu, W.-H. Huang, Q. Zhang, K. Wei, X. Zhou, Y. Zhu, X. Zhong, M.-H. Yeh, N. Alonso-Vante and J. Ma, *Angew. Chem., Int. Ed.*, 2025, **64**, e202511750.
19 X. Mao, M. Zhu, M. Xie, G. Zou, Y. Kuang, S. Guo, J. Hu and X. Xu, *Nano Lett.*, 2025, **25**, 16253–16261.
20 J. Tang, X. Liu, X. Xiong, Q. Zeng, Y. Ji, C. Liu, J. Li, H. Zeng, Y. Dai, X. Zhang, C. Li, H. Peng, Q. Jiang, T. Zheng, C.-W. Pao and C. Xia, *Adv. Mater.*, 2024, **36**, 2407394.
21 S. Zuo, Z.-P. Wu, D. Xu, R. Ahmad, L. Zheng, J. Zhang, L. Zhao, W. Huang, H. A. Qahtani, Y. Han, L. Cavallo and H. Zhang, *Nat. Commun.*, 2024, **15**, 9514.
22 Y. Hao, S.-F. Hung, W.-J. Zeng, Y. Wang, C. Zhang, C.-H. Kuo, L. Wang, S. Zhao, Y. Zhang, H.-Y. Chen and S. Peng, *J. Am. Chem. Soc.*, 2023, **145**, 23659–23669.
23 Q. Yu, Y. Chen, J. Liu, C. Li, J. Hu and X. Xu, *Proc. Natl. Acad. Sci. U. S. A.*, 2024, **121**, e2319894121.
24 G. Luo, M. Song, Q. Zhang, L. An, T. Shen, S. Wang, H. Hu, X. Huang and D. Wang, *Nano-Micro Lett.*, 2024, **16**, 1–36.
25 Z. Lang, X. Wang, S. Jabeen, Y. Cheng, N. Liu, Z. Liu, T. Gan, Z. Zhuang, H. Li and D. Wang, *Adv. Mater.*, 2025, **37**, e2418942.
26 C. Rong, J. Jia, W. Li, S. Wu, Q. Sun, C. Jia, S. Cheong, Y. Guo and C. Zhao, *ACS Catal.*, 2025, **15**, 11705–11715.
27 Y. Liu, Y. Wang, H. Li, M. G. Kim, Z. Duan, K. Talat, J. Y. Lee, M. Wu and H. Lee, *Nat. Commun.*, 2025, **16**, 1717.
28 L. Wang, S.-F. Hung, S. Zhao, Y. Wang, S. Bi, S. Li, J.-J. Ma, C. Zhang, Y. Zhang, L. Li, T.-Y. Chen, H.-Y. Chen, Y. Wu and S. Peng, *Nat. Commun.*, 2025, **16**, 3502.
29 J. Abed, J. Heras-Domingo, R. Y. Sanspeur, M. Luo, W. Alnoush, D. M. Meira, H. Wang, J. Wang, J. Zhou,

D. Zhou, K. Fatih, J. R. Kitchin, D. Higgins, Z. W. Ulissi and E. H. Sargent, *J. Am. Chem. Soc.*, 2024, **146**, 15740–15750.
30 D. Chen, R. Yu, K. Yu, R. Lu, H. Zhao, J. Jiao, Y. Yao, J. Zhu, J. Wu and S. Mu, *Nat. Commun.*, 2024, **15**, 3928.
31 G. Chen, Z. Shang, J. Zhang, X. Li, C. Ma, X. Wang, Y. Xiong and Y. Han, *Angew. Chem., Int. Ed.*, 2025, **65**, e17073.
32 G. Gao, Z. Sun, X. Chen, G. Zhu, B. Sun, Y. Yamauchi and S. Liu, *Appl. Catal., B*, 2024, **343**, 123584.
33 W. Li, D. Chen, Z. Lou, H. Yuan, X. Fu, H. Y. Lin, M. Lin, Y. Hou, H. Qi, P. F. Liu, H. G. Yang and H. Wang, *J. Am. Chem. Soc.*, 2025, **147**, 10446–10458.
34 Y. Dong, Y. Li, Y. Lin, A. Chen, M. Deng, L. Zhang, Z. Tian and L. Chen, *J. Mater. Chem. A*, 2024, **12**, 21905–21911.
35 X. Bai, X. Zhang, Y. Sun, M. Huang, J. Fan, S. Xu and H. Li, *Angew. Chem., Int. Ed.*, 2023, **62**, e202308704.
36 Y. Xu, Z. Mao, J. Zhang, J. Ji, Y. Zou, M. Dong, B. Fu, M. Hu, K. Zhang, Z. Chen, S. Chen, H. Yin, P. Liu and H. Zhao, *Angew. Chem., Int. Ed.*, 2024, **63**, e202316029.
37 K. Khivantsev, N. R. Jaegers, H. Aleksandrov, I. Song, X. Pereira-Hernández, M. Engelhard, J. Tian, L. Chen, D. M. Meira, L. Kovarik, G. Vayssilov, Y. Wang and J. Szanyi, *J. Am. Chem. Soc.*, 2023, **145**, 5029–5040.
38 L. Deng, S.-F. Hung, Z.-Y. Lin, Y. Zhang, C. Zhang, Y. Hao, S. Liu, C.-H. Kuo, H.-Y. Chen, J. Peng, J. Wang and S. Peng, *Adv. Mater.*, 2023, **35**, 2305939.
39 N. Deka, T. E. Jones, L. J. Falling, L.-E. Sandoval-Diaz, T. Lunkenbein, J.-J. Velasco-Velez, T.-S. Chan, C.-H. Chuang, A. Knop-Gericke and R. V. Mom, *ACS Catal.*, 2023, **13**, 7488–7498.
40 A. Kumar, M. Gil-Sepulcre, J. Lee, V. Q. Bui, Y. Wang, O. Ruediger, M. G. Kim, S. DeBeer and H. Tuysuz, *Adv. Mater.*, 2024, **36**, 2401648.
41 Q. Lu, J. Liu, X. Zou, B. Huang, W. Wu, J. Yin and Z.-Q. Liu, *Angew. Chem., Int. Ed.*, 2025, **64**, e202503733.
42 L. Wu, W. Huang, D. Li, B. Zhao, H. Zhou and W. Luo, *Angew. Chem., Int. Ed.*, 2025, **64**, e202420848.
43 F. Qian, D. Cao, S. Chen, Y. Yuan, K. Chen, P. J. Chimtali, H. Liu, W. Jiang, B. Sheng, L. Yi, J. Huang, C. Hu, H. Lei, X. Wu, Z. Wen, Q. Chen and L. Song, *Nat. Commun.*, 2025, **16**, 6894.
44 Q. Ji, B. Tang, X. Zhang, C. Wang, H. Tan, J. Zhao, R. Liu, M. Sun, H. Liu, C. Jiang, J. Zeng, X. Cai and W. Yan, *Nat. Commun.*, 2024, **15**, 8089.
45 W. Zhang, C. Zhu, Y. Wen, M. Wang, Z. Lu and Y. Wang, *Angew. Chem., Int. Ed.*, 2024, **137**, e202418456.
46 J. Chang, Y. Shi, H. Wu, J. Yu, W. Jing, S. Wang, G. I. N. Waterhouse, Z. Tang and S. Lu, *J. Am. Chem. Soc.*, 2024, **146**, 12958–12968.
47 X. Luo, H. Zhao, X. Tan, S. Lin, K. Yu, X. Mu, Z. Tao, P. Ji and S. Mu, *Nat. Commun.*, 2024, **15**, 8293.
48 X. Cao, H. Qin, X. Chen and L. Jiao, *J. Am. Chem. Soc.*, 2024, **146**, 32049–32058.
49 H. Wang, C. Lin, L. Tan, J. Shen, X. Wu, X. Pan, Y. Zhao, H. Zhang, B. Mei, H.-D. Um, Q. Xiao, W. Jiang, X. Li and W. Luo, *Nat. Commun.*, 2025, **16**, 3976.
50 M. Qi, X. Du, X. Shi, S. Wang, B. Lu, J. Chen, S. Mao, H. Zhang and Y. Wang, *J. Am. Chem. Soc.*, 2025, **147**, 18295–18306.
51 M.-R. Qu, H. Liu, S.-H. Feng, X.-Z. Su, J. Xu, H.-L. Duan, R.-Q. Liu, Y.-Y. Qin, W.-S. Yan, S. Zhu, R. Wu, H. Li and S.-H. Yu, *Nat. Commun.*, 2025, **16**, 9261.
52 Y. Mu, J. Fan, T. Gao, L. Wang, L. Zhang, X. Zou, W. Zheng, Y.-W. Zhang, Z. G. Yu and X. Cui, *Angew. Chem., Int. Ed.*, 2025, **64**, e202504876.
53 Y. Chen, Q. Li, Y. Lin, J. Liu, J. Pan, J. Hu and X. Xu, *Nat. Commun.*, 2024, **15**, 7278.
54 X. Cao, H. Qin, J. Zhang, X. Chen and L. Jiao, *J. Am. Chem. Soc.*, 2024, **146**, 32049–32058.
55 L. Wu, W. Huang, D. Li, H. Jia, B. Zhao, J. Zhu, H. Zhou and W. Luo, *Angew. Chem., Int. Ed.*, 2024, **64**, e202413334.
56 L. Deng, H. Chen, S.-F. Hung, Y. Zhang, H. Yu, H.-Y. Chen, L. Li and S. Peng, *J. Am. Chem. Soc.*, 2024, **146**, 35438–35448.
57 X. Chen, X.-T. Wang, J.-B. Le, S.-M. Li, X. Wang, Y.-J. Zhang, P. Radjenovic, Y. Zhao, Y.-H. Wang, X.-M. Lin, J.-C. Dong and J.-F. Li, *Nat. Commun.*, 2023, **14**, 5289.
58 J. Zhu, X. Sun, N. Feng, B. Zhao, M. Qiu, J. Xu and W. Luo, *J. Am. Chem. Soc.*, 2025, **147**, 47454–47466.
59 Y. Yokoyama, K. Miyazaki, Y. Kondo, Y. Miyahara, T. Fukutsuka and T. Abe, *Chem. Lett.*, 2020, **49**, 195–198.
60 L. Li, G. Zhang, J. Xu, H. He, B. Wang, Z. Yang and S. Yang, *Adv. Funct. Mater.*, 2023, **33**, 2213304.
61 J. Wang, Y. Zhang, S. Jiang, C. Sun and S. Song, *Angew. Chem., Int. Ed.*, 2023, **62**, e202307808.
62 C. Lin, J. Li, X. Li, S. Yang, W. Luo, Y. Zhang, S.-H. Kim, D.-H. Kim, S. S. Shinde, Y.-F. Li, Z.-P. Liu, Z. Jiang and J.-H. Lee, *Nat. Catal.*, 2021, **4**, 1012–1023.
63 S. G. H. Kumar, C. Bozal-Ginesta, N. Wang, J. Abed, C. H. Shan, Z. Yao and A. Aspuru-Guzik, *Chem. Sci.*, 2024, **15**, 10556–10570.
64 Y. a. Zhu, F. Wu, X. Zhang, Y. Lin, L. Zhang, T.-S. Chan, Q. Zhang and L. Chen, *Adv. Mater.*, 2025, **37**, 2500449.
65 H. Wang, T. Zhai, Y. Wu, T. Zhou, B. Zhou, C. Shang and Z. Guo, *Adv. Sci.*, 2023, **10**, 2301706.
66 Q. Zhang, W. Zhang, J. Zhu, X. Zhou, G.-R. Xu, D. Chen, Z. Wu and L. Wang, *Adv. Energy Mater.*, 2024, **14**, 2304546.